

Research Paper

Vermiculate artefacts in image analysis of granular materials



Sam Stanier ^{a,*}, Jelke Dijkstra ^b, Danuta Leśniewska ^c, James Hambleton ^d, David White ^a,
David Muir Wood ^{e,b,a}

^a Centre for Offshore Foundation Systems, University of Western Australia, Australia

^b Division of Geo-engineering, Chalmers Tekniska Högskola, Göteborg, Sweden

^c Politechnika Koszalińska, Koszalin, Poland

^d Department of Civil Engineering, Newcastle University, New South Wales, Australia

^e Division of Civil Engineering, University of Dundee, United Kingdom

ARTICLE INFO

Article history:

Received 21 May 2015

Received in revised form 24 September 2015

Accepted 11 November 2015

Available online 8 December 2015

Keywords:

Granular materials

Digital image correlation

Vermiculation

Sub-pixel interpolation

ABSTRACT

Some reported analyses of images of deforming granular materials have generated surprising vermiculate strain features which are difficult to reconcile with the mechanics of deformation of granular matter. Detailed investigation using synthetic images and improved processing of images of laboratory experiments indicates that such features can emerge as a consequence of the image acquisition (sensor, contrast, resolution), the subsequent image correlation implementation, and the user's choice of processing parameters. The two principal factors are: (i) the texture and resolution of the images and (ii) the algorithm used to achieve sub-pixel displacement resolution. Analysis of the images using a sub-pixel interpolation algorithm that is more robust than that used originally eliminates the vermiculate features for images with moderate resolution and texture. However, erroneous features persist in images with low resolution and poor texture. Guidance is provided on ways in which such artefacts can be avoided through improved experimental and image analysis techniques.

© 2015 Elsevier Ltd. All rights reserved.

1. Introduction

Image analysis has become a widely used tool for obtaining full-field information of displacements in granular media. The process starts with the design of an experiment that allows the acquisition of digital images of the deforming material (e.g. behind a transparent window) at chosen intervals. Example experimental setups have been described for element testing [4], large scale 1 g testing [40] and centrifuge testing [28]. Similar equipment has been used to capture images to investigate a wide range of geotechnical phenomena, including: the development of shear bands in sands [23]; seasonal rainfall-induced slope failures [33]; the effects of tunnelling in sand on greenfield settlements [14]; and fault rupture propagation in sand [2].

Several image processing techniques have been developed to deduce displacements from analysis of successive images captured using such experimental apparatus, e.g. image subtraction [10,24], particle tracking [7,3] and image correlation techniques such as Particle Image Velocimetry (PIV) [38,41] and Digital Image Correlation (DIC) [31]. With adequate image texture (the number and contrast of spatial features and/or grains), image correlation

techniques are most suitable for obtaining accurate displacement fields with high spatial resolution.

However, it is not trivial to retrieve meaningful displacement data from such experiments. The quality of the image texture (or speckle pattern) is typically dictated by: (i) the natural contrast of coarse grained material or the artificial seeding applied to the surface of the specimen that is visible to the digital camera through a transparent window (which is dependent on the scale or resolution of the image because this determines how well individual grains can be distinguished); (ii) the image acquisition process (sensor, lens, illumination, field of view and image capture frequency); and (iii) any image pre-processing applied prior to the displacement computations. In addition, the image correlation algorithm chosen to compute the displacements needs to be carefully selected in order to avoid numerical artefacts in the image analyses.

Muir Wood and Leśniewska [15] and Nazhat and Airey [16] provide examples of analyses that have potentially been affected by erroneous numerical artefacts that appear in the strain fields computed from the displacements as highly concentrated bands of shearing. Such features are difficult to reconcile with the mechanics of deformation of granular matter. This paper aims to provide guidance on the selection of the most influential experimental

* Corresponding author.

parameters in order to avoid spurious features and presents some examples of features that might arise for ill-chosen conditions.

2. Image correlation: a brief description

The tools employed in geotechnical applications of image analysis have either been developed within the community [41,9] or have been borrowed from adjacent disciplines, e.g. open source PIV tools such as MatPIV [32], PIVlab [35], OpenPIV [34] and JPIV [37]. Meanwhile developments in experimental mechanics and fluid mechanics continue [17,25].

The ability to extract displacement fields from image correlation rests on four implicit assumptions [1]:

- The particles that are observed are homogeneously distributed across the image. This will usually be automatically satisfied for sands, where the individual grains often contain sufficient natural colour variation to provide adequate contrast. For clay models individual particles are not visible and a (homogeneous) surface speckle has to be added by artificial seeding.
- The observed natural or imposed image texture provides a perfect representation of the displacement of the soil. Wall friction may make the observed displacements unrepresentative of the displacements occurring through the thickness of the material.
- The ‘reference’ and ‘target’ images are sufficiently similar (i.e. the deformation is small enough) that a spatial measure of correlation can be computed and a clear peak isolated for all subsets (also known as patches or interrogation windows).
- The shape (or warp) function (which mathematically describes how the subset is allowed to displace and deform during the displacement computation) used by the image correlation algorithm should be consistent with the deformation being measured. Simpler correlation algorithms assume that the transformation from ‘reference’ to ‘target’ is a pure translation; more sophisticated algorithms may accept distortion or rotation in addition to translation.

Most freely available PIV/DIC algorithms, including those referenced here, perform two separate computations: (i) selection of a subset within the ‘reference’ image for which the peak in cross-correlation can be sought in successive ‘target’ images, for each subset, to the nearest integer pixel coordinates; and (ii) refinement of this measurement by interpolation of the cross-correlation for the subset corresponding to the correlation peak and a selection of its neighbours in order to refine the displacement measurement to sub-pixel resolution. Algorithms which employ a zero-order subset shape function which only permits the subset to be translated when seeking to maximise the cross-correlation cannot accommodate significant distortion or rotation. Large gradients of displacement across the subset being interrogated can lead to an inability to correlate ‘reference’ and ‘target’ images, inevitably resulting in measurement errors.

2.1. Cross-correlation of the subsets

Subsets of an initial ‘reference’ image are compared with subsequent ‘target’ images in order to calculate a spatial measure of cross-correlation (CC) (see Fig. 1). Two popular measures are ‘normalised cross-correlation’ (NCC) [13] and ‘zero normalised cross-correlation’ (ZNCC) [20]. The zero normalised cross-correlation coefficient (CC_{ZNCC}) represents a robust measure of correlation as it can accommodate variations (offset and/or scale) in brightness across the image, with values of 1, 0 and –1 indicating perfect, zero and inverse correlation, respectively. Mathematical definitions for

CC_{ZNCC} and other measures used throughout this paper are provided in the Appendix A.

2.2. Sub-pixel displacement refinement

The integer displacement estimate from the first step is refined using sub-pixel interpolation functions. Typically bi-cubic splines or Gaussian functions are fitted to the correlation peak and the neighbouring values (Fig. 2). The maximum value of the interpolant provides an improved estimate of displacement typically to sub-pixel precision of the order of $0.01p$ [41], where p is the pixel size.

More sophisticated sub-pixel displacement refinement can be achieved by incorporating more complex basis spline curve-fitting of the interpolation peak [11]. Alternatively, a higher-order subset shape function that allows the displacements within the subset to vary linearly or non-linearly for first- and second-order shape functions respectively [42], could be incorporated. Methods with higher-order subset shape functions tend to deal with spatially varying deformation fields more robustly but require additional image intensity interpolation and optimisation techniques and have until recently not been widely available. Ncorr [5] and GeoPIV-RG [27] are two recently developed examples of PIV/DIC software which incorporate such an enhanced sub-pixel displacement refinement and which are now freely available to the geotechnical research community.

3. Requirements for accurate cross-correlation

The following design rules are based on experiences in fluid mechanics using PIV to analyse the trajectories of tracers in fluid flow (e.g. [1]), DIC analysis of a speckle pattern on a material surface (e.g. [30]), and recent experience of performing PIV/DIC analyses on various laboratory geomaterials (e.g. [28]).

R1 Image quality: A large Signal-to-Noise Ratio (SNR) (see Appendix A for definition) using the full dynamic range of the image sensor is desirable. Provide sufficient and uniform illumination of the specimen. Use high quality optics characterised by a small available f-stop (absence of optical aberrations); then set aperture with the highest value of f-stop (smallest aperture size) compatible with the available illumination and desired depth of field. Select a camera with a global rather than rolling shutter, and with a Charge-Coupled Device (CCD) sensor rather than a Complementary Metal Oxide Semiconductor (CMOS) sensor [28]. Images with a uniform distribution in the intensity histogram with values between 20 and 225 are considered high quality for an 8-bit sensor (maximum 255 intensity levels). Values lower than 20 are often associated with sensor noise, whilst values above 220 are approaching sensor saturation [30]. Image formats with high compression will reduce the SNR of the image (e.g. [6]). Uneven or fluctuating illumination has a large impact on the subsequent analysis if non-normalised cross-correlation is used (e.g. [36]). Quantitative assessment of global image quality can be provided by checking the Mean Intensity Gradient (MIG) proposed by Pan et al. [18].

R2 Information in the signal: The spatial resolution of the digital image data, stored in a pixel array, where each pixel holds an intensity value for the amount of light that fell on that pixel, is discrete. Hence, there should be a sufficient number of pixels in the spatial feature that needs to be followed, for example the grain, in order to retain enough information in the signal. Theoretical and experimental analysis from

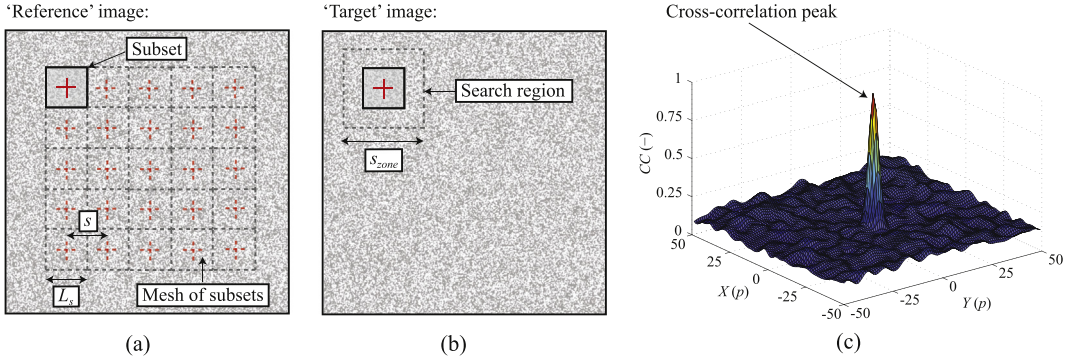


Fig. 1. Schematic diagram of typical PIV/DIC computations: (a) definition of mesh of subsets on 'reference' image, (b) computation of cross-correlation (CC) over a region encompassing the subset in the 'target' image, and (c) location of the peak in cross-correlation to the nearest integer pixel values.

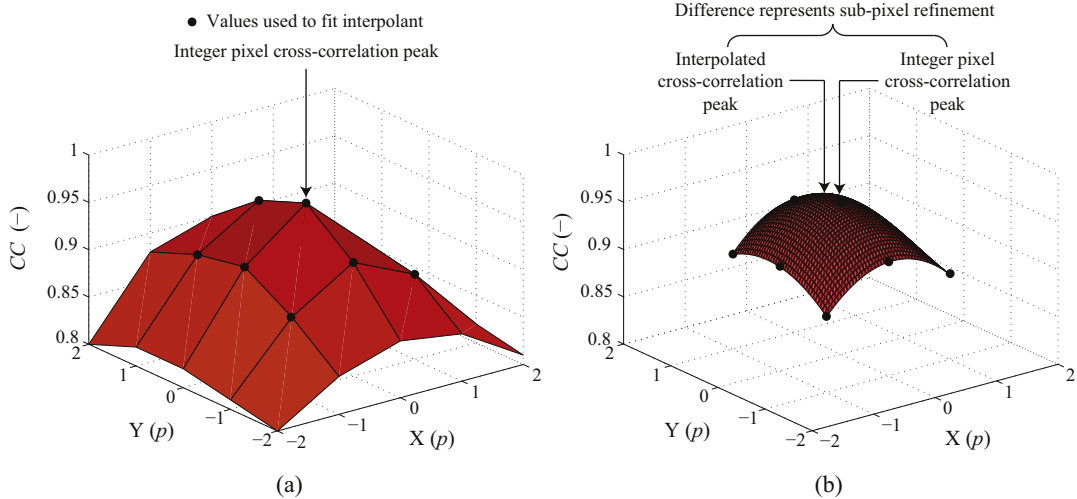


Fig. 2. Conventional sub-pixel refinement: (a) isolation of the cross-correlation peak and values for neighbouring subsets (at integer pixel locations) and (b) bi-cubic interpolation of the cross-correlation peak and the eight nearest neighbours to identify an interpolated peak to sub-pixel resolution.

fluid mechanics has shown that this requires 2 pixels across each particle [39], implying that for soils $d_{50}/p \sim 2$, where d_{50} is the median grain size. Fewer pixels will not resolve the grain and more pixels will increase the noise unless the observed surfaces of the grains show adequate contrast. In solid mechanics where higher seeding densities (denser speckles) are more common the average recommended feature size is doubled, to 4×4 pixels. Sutton [30] introduces a more systematic way of determining the feature size of the speckle in an image by performing autocorrelation and recommends sizes of 3×3 to 7×7 pixels.

- R3 *Texture or speckle quality:* The grains, or imposed speckle, should provide sufficient contrast between the particles contained within the subsets. The intensity differences between the grains and the voids should be larger than the noise in the image. In medical imaging this feature is sometimes called contrast resolution [29]. This requirement is readily satisfied when images with high SNR and materials with distinct colour differences are used. In geotechnical applications Stanier and White [28] recommend that seeding be applied to models such that: (i) the Artificial Seeding Ratio is in the range of $0.3 < ASR < 0.7$ (see Fig. 3) so as to ensure an optimal quantity of seeding has been applied to the model; and (ii) the standard deviation of the subset intensities σ_{I_s} is greater than 15 so as to ensure that there is sufficient contrast within the subsets. The Sum of Squares

of Subset pixel Intensity Gradients (SSSIG) provides another alternative measure of subset quality with a minimum threshold for precise measurements of $SSSIG > \sim 1 \times 10^5$ recommended by Pan et al. [21].

R4 *Subset size:* For geotechnical purposes it is recommended that each subset should contain a minimum of 10 contrasting particles (whether sand grains or artificial seeding such as modelling flock) in each direction (so that the total number of particles, $n > \sim 100$), so as to increase the likelihood that the real displacement of the subset of soil can be extracted. At the same time the subset should be sufficiently small for the order of its shape function to be consistent with the deformation being measured. Higher-order (first- or second-order) shape functions improve correlation of subsets which undergo spatially varying deformations and thus allow the use of larger subsets, which will typically contain more information and provide more robust correlations. In practice, a subset size of 24×24 to 48×48 pixels provides a good starting point from which trial and error refinement can be performed if deemed necessary.

R5 *Subset overlap:* Overlapping of subsets for adjacent points permits more data to be obtained from the image resulting in increased spatial resolution (i.e. over-sampling; see Fig. 4). However, bias errors can arise when the subset shape function is incompatible with the deformation of the subset that is being measured [26]. Overlapping can amplify the

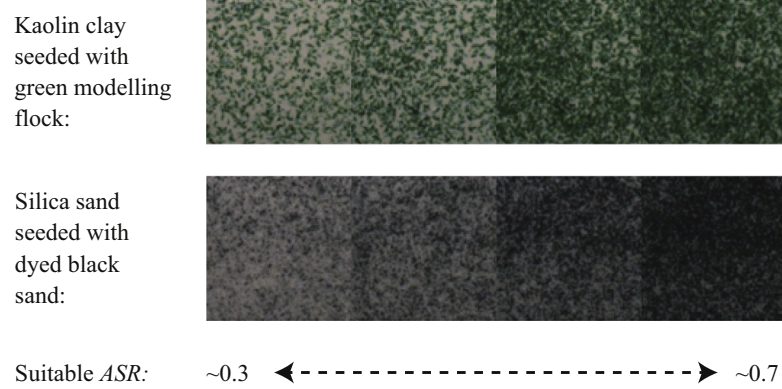


Fig. 3. Examples of suitable Artificial Seeding Ratio (ASR) for Kaolin clay and Silica sand after Stanier and White [28].

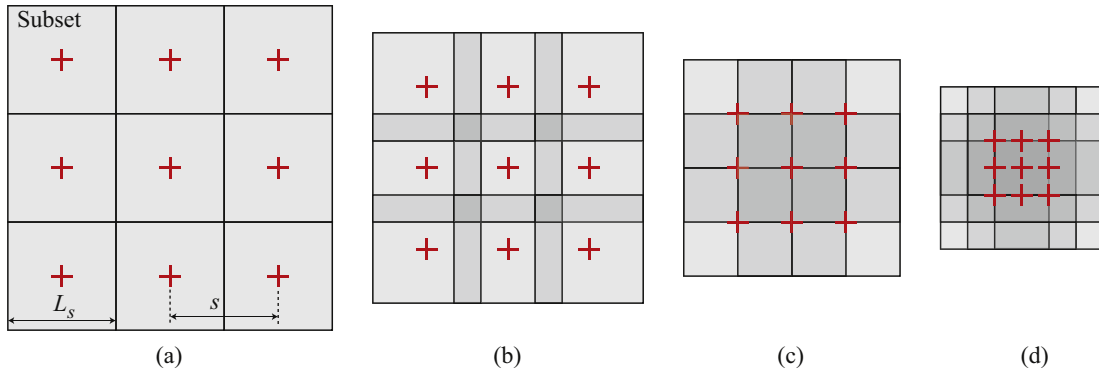


Fig. 4. Subset of size $L_s \times L_s$ at spacings of s for overlapping ratios $((L_s - s)/L_s)$ of: (a) 0.0, (b) 0.25, (c) 0.5 and (d) 0.75. Darker regions represent oversampling caused by increasing overlap, resulting in increased spatial resolution.

error in computing strains from the derivatives of the displacement fields [22]. In fluid dynamics overlap ratios of 0.2 to 0.5 are recommended as a good compromise between maximising the number of measurement points and minimising the impact of potential bias in the displacement field. Plotting histograms of either the total or sub-pixel displacement component magnitudes provides a ready check for the presence of bias errors. Bias is evident when saw-toothed total displacements or non-uniform sub-pixel displacement distributions are apparent (see Fig. 5 and Raffel et al. [22]): the locking of displacement peaks onto integer pixel values of displacement (Fig. 5(a)) is unlikely to be a realistic representation of the actual displacement field.

R6 Deformation magnitude: For basic PIV/DIC implementations that do not allow the subsets to deform (i.e. zero-order subset shape function), the maximum deformation or strain occurring between two cross-correlated images should not be too large. In some of the experimental observations presented later in Section 5, relatively large deformations are observed between successively captured image pairs (engineering shear strains $\gamma > 30\%$) leading to persistent bias errors. In practice the deformation experienced within the subsets between the ‘reference’ and ‘target’ images should be limited to preserve the correlation as well as minimising the area over which the correlation measure is to be computed, which generally results in less computational expense. This can be achieved by capturing additional images at intermediate intervals. Algorithms that use higher-order subset shape functions (e.g. [5,27]) and image intensity interpolation and optimisation to achieve

sub-pixel measurement resolution can tolerate greater deformations before decorrelation leads to erroneous measurements. Automatic ‘reference’ image updating schemes that use the correlation coefficients of the subsets to decide when to update the ‘reference’ image, such as those described by Pan et al. [19] and Stanier et al. [27], can be used to process the additional images in an optimised manner. These methods tend to be more computationally intensive for single computations; however, preconditioning of the optimisation problem for each subset by assimilation of information from the neighbouring subset having the best correlation leads to vastly improved efficiency for subsequent computations. It is then unnecessary to calculate the initial measure of correlation over large areas of the ‘reference’ and ‘target’ images for every subset.

4. Spurious features: synthetic data

The following synthetic analyses demonstrate that numerical artefacts can appear in PIV/DIC analyses of geomaterial if the particles or features that make up the image texture are too small relative to the pixel size in the images captured (contravening rule R3), causing the sub-pixel refinement process to break down. Synthetic images containing single particles of different sizes were generated, displaced by sub-pixel distances and subsequently analysed using zero-order PIV/DIC techniques. The synthetic images were 25×25 pixels in size, with a black background onto which white dots with varying brightness of Gaussian distribution were projected to sub-pixel precision. The intensities of each pixel in the images were estimated from the Gaussian distribution

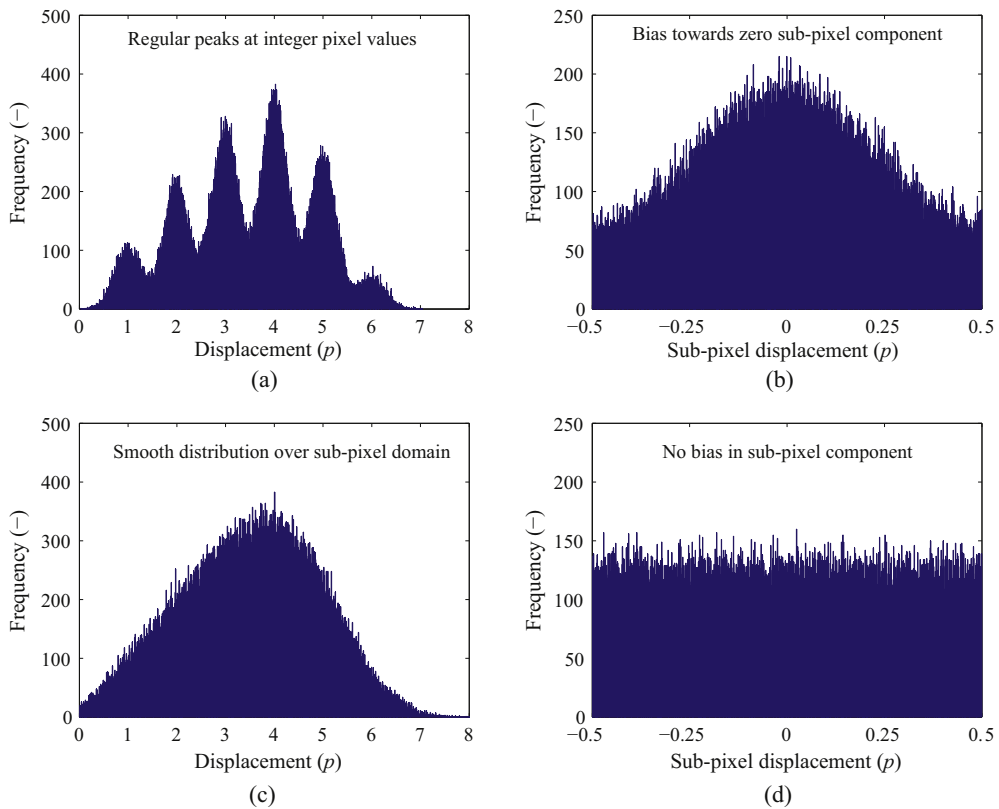


Fig. 5. Histograms of displacement magnitudes: (a and b) total and sub-pixel displacement components with bias errors and (c and d) total and sub-pixel displacement components without bias errors.

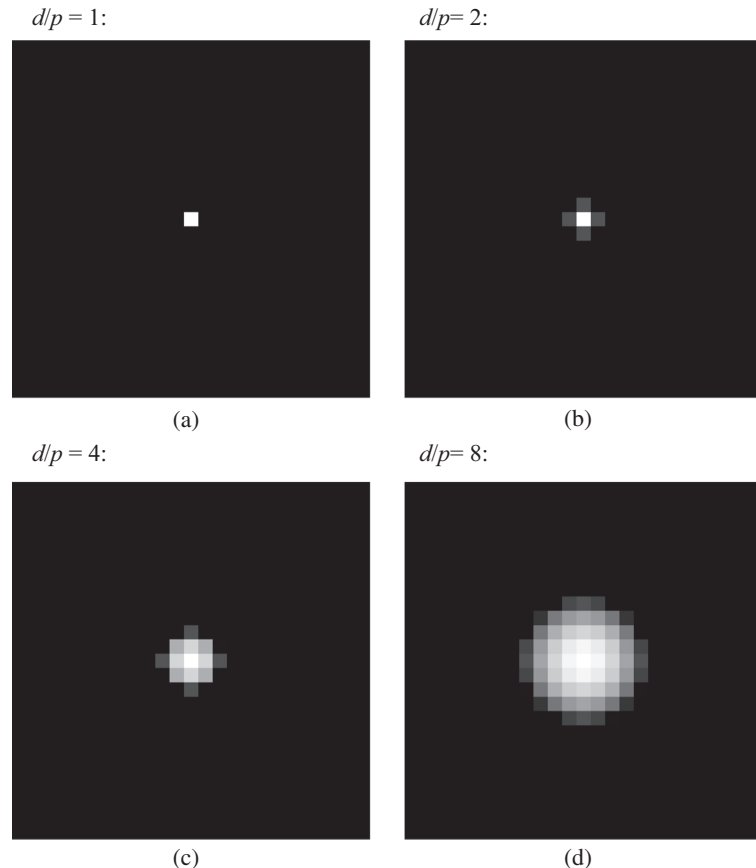


Fig. 6. Example images for the single particle displacement analysis with particle/pixel size ratios: (a) $d/p = 1$; (b) $d/p = 2$; (c) $d/p = 4$; and (d) $d/p = 8$.

describing the brightness of the dot (see the [Appendix A](#) for a mathematical definition). [Fig. 6](#) shows the four initial images generated by this process for dot sizes, $d = p, 2p, 4p$ and $8p$. The dot in the ‘reference’ image was then displaced horizontally in increments $\delta x = 0.02p$ over the range of $-0.5p < \delta x < 0.5p$. The zero normalised cross-correlation coefficient (CC_{ZNCC}) was calculated for a centrally located 15×15 pixel subset and the eight neighbouring subsets using Eq. (1) see [Appendix A](#).

A bi-cubic interpolant was fitted to the correlation surface described by the CC_{ZNCC} values of the subsets and sampled at intervals of 0.005 pixels (i.e. the smallest non-zero displacement that could possibly be measured was 0.005 pixels). The location of the peak of the interpolant, which provides the best estimate of the displacement to sub-pixel resolution, is compared with the imposed displacement in [Fig. 7](#) for particle/pixel size ratio $d/p = 1, 2, 4$ and 8 . [Fig. 8](#) presents cross sections of the interpolated correlation peak at displacement increments, $\delta x = -0.4p, 0$ and $0.3p$ with the inferred and imposed displacements indicated by dashed and solid lines respectively.

When d/p is small, there is a bias in the computed displacements towards the integer pixel value closest to the correlation peak (zero in the present example), and the inferred and imposed displacements diverge for non-zero displacements ([Fig. 7](#)). The interpolant has a sharp peak because the neighbouring subsets have very poor correlation by comparison with this centrally located peak correlation ([Fig. 8](#)). This phenomenon is known as ‘peak locking’ [38]. As d/p increases the correlation in the neighbouring subsets improves causing the interpolated correlation peak to shift location. As a result, the bias reduces and the displacements inferred are much closer to those imposed. However, if the grains are of uniform colour, and have a high d/p ratio, (so that there are several pixels in a single particle), then undesirable ‘correlation noise’ can develop with many spurious peaks (see rule R3). We can imagine three cases: with small d/p the cross-correlation function has a sharp peak which cannot be refined by sub-pixel interpolation; with large d/p but with grains which lack contrast the correlation function is noisy; with large d/p and with contrasting grain texture the correlation should be optimal.

In order to demonstrate the impact that ‘peak locking’ can have on strain field computations involving geomaterials, an artificial smooth displacement field was imposed on synthetic soil-like images. The initial ‘reference’ images were generated by randomly projecting thousands of white dots – each with intensity described numerically by a Gaussian curve (see the [Appendix A](#) for a mathematical definition), as in the previous section – onto a black background. Sufficient dots were projected until each image had a mean pixel intensity of ~ 125 (for a gray scale image intensity ranging from 0 to 255). This ensured that each image had the same amount of pixel information, but the images were arranged in different ways. In each analysis the dots were all of the same size, but analyses were run with dot diameters between 1 and 10 pixels in 0.25 pixel increments. [Fig. 9](#) shows four of the images generated with particle to pixel size ratios $d/p = 1, 2, 4$ and 8 respectively. A Flamant displacement field [8] was then imposed onto the ‘reference’ positions of the dots to create a ‘target’ image for each value of d/p ([Fig. 10](#)). This smoothly varying displacement field contains both supra- and sub-pixel displacement magnitudes and implies correspondingly smooth variations of engineering shear strain, γ .

The displacement fields between each pair of images were analysed using both GeoPIV and the first-order subset deformation variant GeoPIV-RG [27]. The analysis control parameters adopted for both algorithms are given in [Table 1](#). [Fig. 11](#) presents the fields of engineering shear strain, γ , for particle size ratios $d/p = 1, 2, 4$ and 8 computed using GeoPIV and GeoPIV-RG. Spurious features are clearly evident for the GeoPIV analyses for the smallest

particles but these disappear as the particle size d/p increases. Examination of the displacement fields reveals that these features are always located where the true displacement is a half-integer value $\delta x = mp/2$ ($m \in \mathbb{Z}$). The interpolation process has failed and the sub-pixel interpolation step essentially recovers the nearest integer pixel value (cf. [Fig. 7](#)). As the particle size rises to $d/p = 8$ the spurious features largely disappear, but the strain fields have noise of $\sim 1\%$. The GeoPIV-RG analyses only show the spurious features for $d/p < 2$ (the theoretical limit derived by Westerweel [39]), but these are less pronounced than for the GeoPIV analysis. [Fig. 12](#) shows that the optimal correlation coefficient (CC_{ZNCC}) output by GeoPIV-RG is much higher than that computed for the zero-order subset deformation analyses of GeoPIV, where CC_{ZNCC}

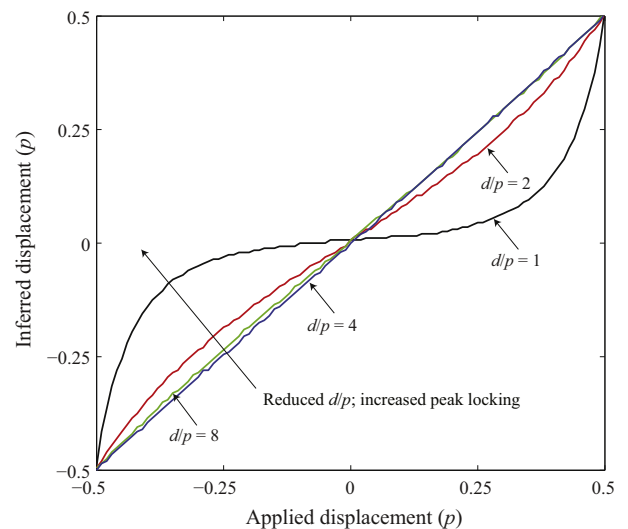


Fig. 7. Impact of particle/pixel size ratio, d/p , on the difference between inferred and actual displacement.

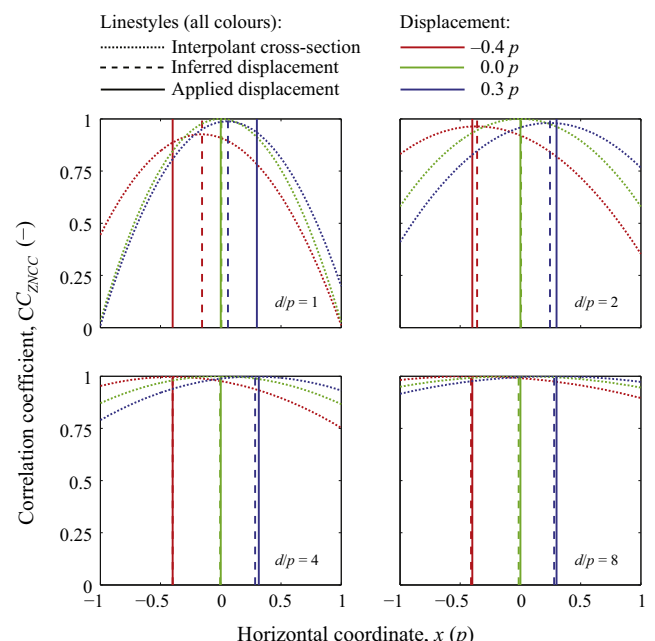


Fig. 8. Impact of particle/pixel size ratio, d/p , on the shape and bias of the bi-cubic interpolant fitted to the correlation coefficient (CC_{ZNCC}) peak and its eight nearest neighbours to achieve sub-pixel measurement resolution.

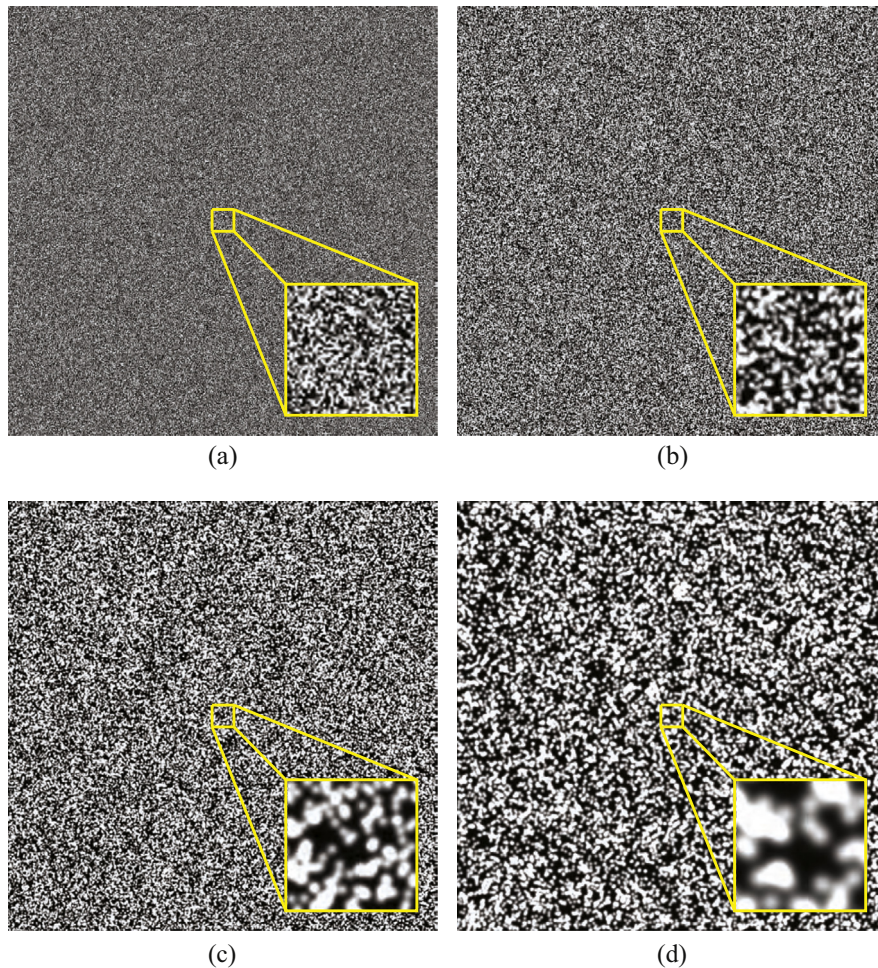


Fig. 9. Randomly generated synthetic images with ASR ~ 0.5 [28] with zoomed inset of approximate subset size (45×45 pixels) highlighted: particle/pixel size ratios: (a) $d/p = 1$; (b) $d/p = 2$; (c) $d/p = 4$; and (d) $d/p = 8$.

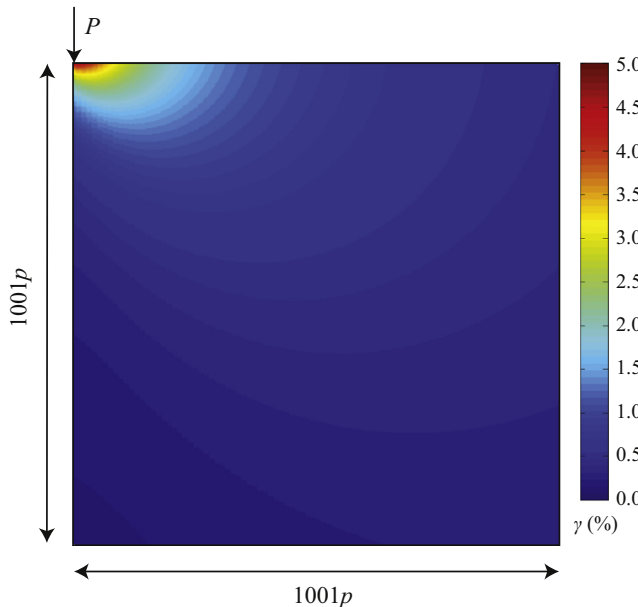


Fig. 10. Engineering shear strain field, γ , generated for a Flamant displacement field with an arbitrary value for the point force, P .

degrades as the deformation magnitude rises. The improved algorithms are significantly less susceptible to 'peak locking' and much more precise.

Table 1
GeoPIV and GeoPIV-RG analysis settings.

GeoPIV ^a	
L_s	$48p \times 48p^c$
s	$12p$
s_{zone}	$15p$
GeoPIV-RG ^b	
D_s	$54p^c$
s	$12p$
\max_{iter}	50
$ \Delta p _{max}$	1×10^{-5}
$CC_{ZNCC-seed-tol}$	0.9
$CC_{ZNCC-max-tol}$	0.75

^a s_{zone} is the search zone over which the cross-correlation function is estimated for each subset, as illustrated in Fig. 1 and described by White et al. [41].

^b \max_{iter} is the maximum number of deformation parameter optimisation iterations; $|\Delta p|_{max}$ is the norm of the warp function difference which is used as an exit criterion for the deformation parameter optimisation process with small values indicating that an optimised solution has been found; $CC_{ZNCC-seed-tol}$ is the tolerance on the correlation coefficient for the seed computation and $CC_{ZNCC-max-tol}$ is the tolerance on the correlation coefficient for the full displacement field. See Stanier et al. [27] for further details.

^c Subset sizes chosen to have near equivalent area (within $\sim 0.6\%$).

5. Spurious features: real data

Reporting of surprising vermiculate strain features in model tests described by Muir Wood and Leśniewska [15] and by Nazhat and Airey [16] provided the initial impetus for the studies reported

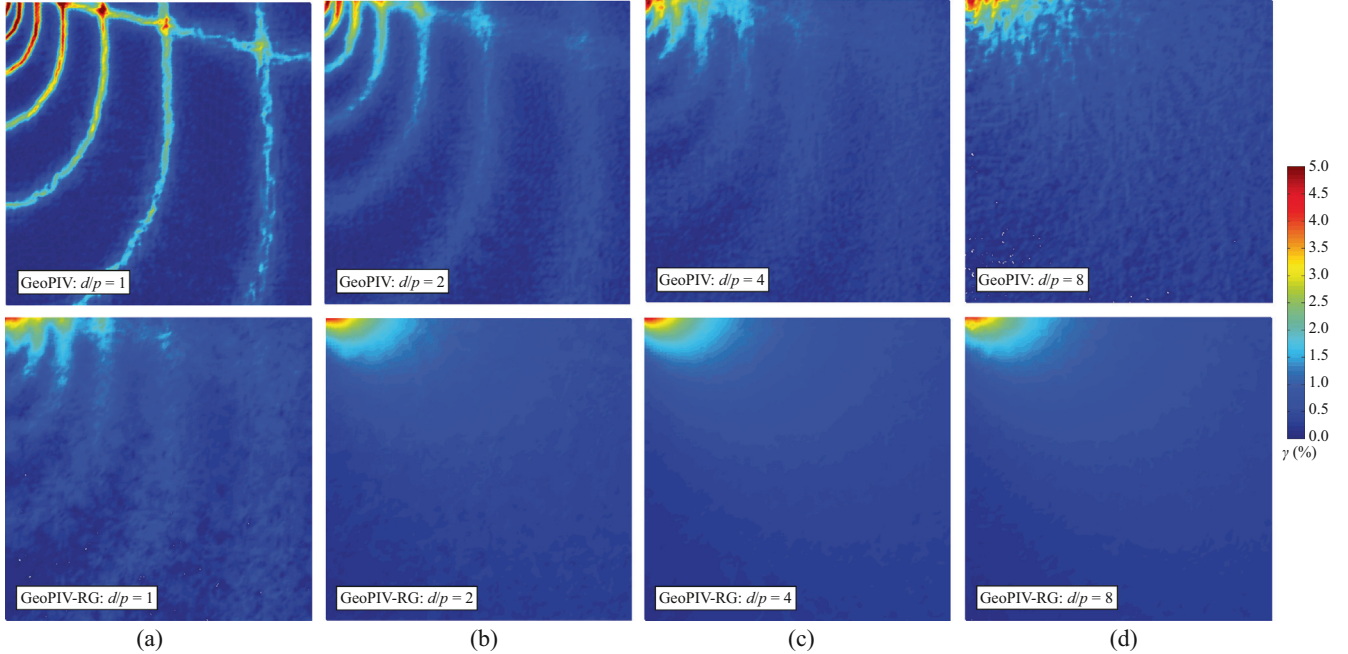


Fig. 11. Engineering shear strain fields, γ , obtained using GeoPIV and GeoPIV-RG for synthetic images with an imposed Flamant displacement field (cf. Fig. 10): particle/pixel size ratios: (a) $d/p = 1$; (b) $d/p = 2$; (c) $d/p = 4$; and (d) $d/p = 8$.

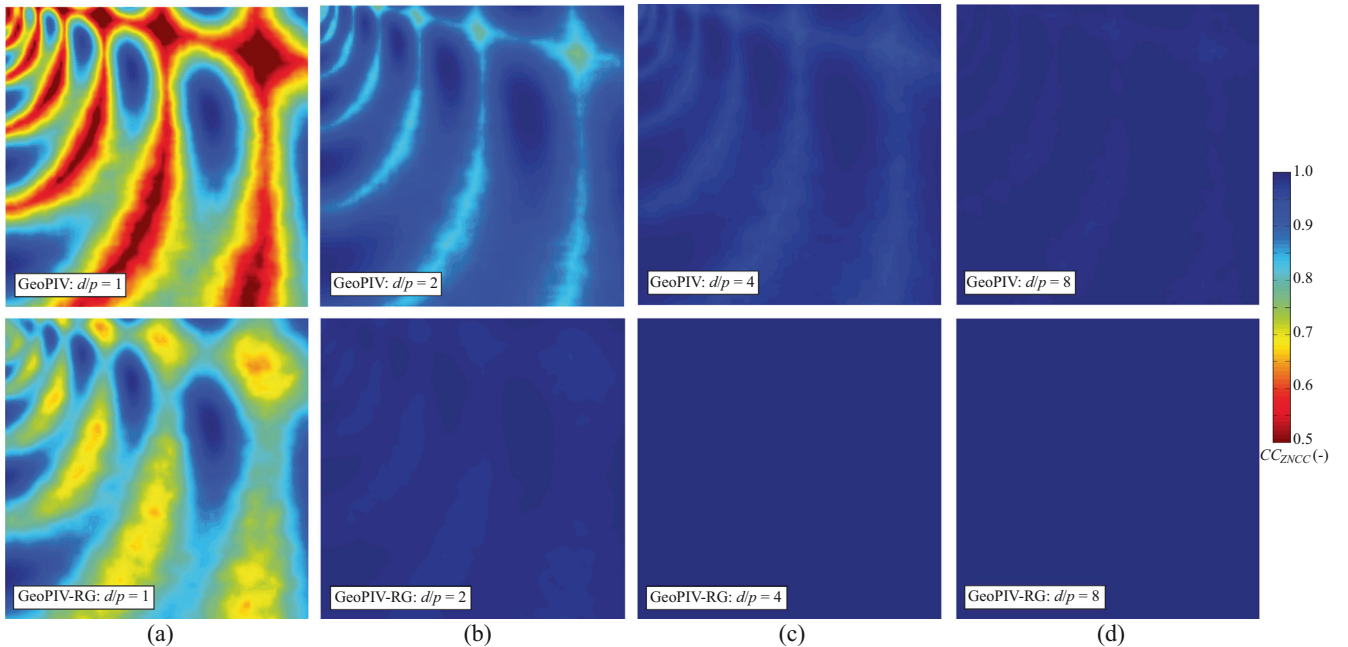


Fig. 12. Optimal zero normalised cross-correlation coefficients, CC_{ZNCC} , obtained using GeoPIV and GeoPIV-RG for synthetic images with an imposed Flamant displacement field: particle/pixel size ratios: (a) $d/p = 1$; (b) $d/p = 2$; (c) $d/p = 4$; and (d) $d/p = 8$.

in this paper. Leśniewska and Muir Wood [12] observed glass ballotini, of 1 mm diameter, contained in a box approximately $200 \times 200 \times 20$ mm. A series of articulated footings applied a controlled stress to the surface of the granular material (Fig. 13). The material was retained by a wall whose outward translation could be controlled, producing deliberate rotation of principal axes of strain. The particles were immersed in a fluid with closely matched refractive index so that when observed with polarised light the photoelastic properties of the glass particles could be exploited to obtain information connected to the stress state in the granular material. The texture of the glass ballotini seen with transmitted light was used in PIV/DIC analysis of the displacement fields. In

these images the contrast is lower than it might be if the pores were filled with air or water but the displacement fields deduced are much less influenced by possible wall friction because the received light has passed through the full thickness of the model.¹

¹ As a relevant detailed comment, the later images were obtained using glass beads which had been annealed, leaving them essentially stress free, and making the model almost perfectly transparent. Previous tests had been performed using the same kind of glass beads, but in their original unannealed state. Thermal tempering (rapid cooling) of these particles left traces of tensile internal stress in each individual grain, making their assembly less transparent in ordinary light and much less transparent in polarised light.

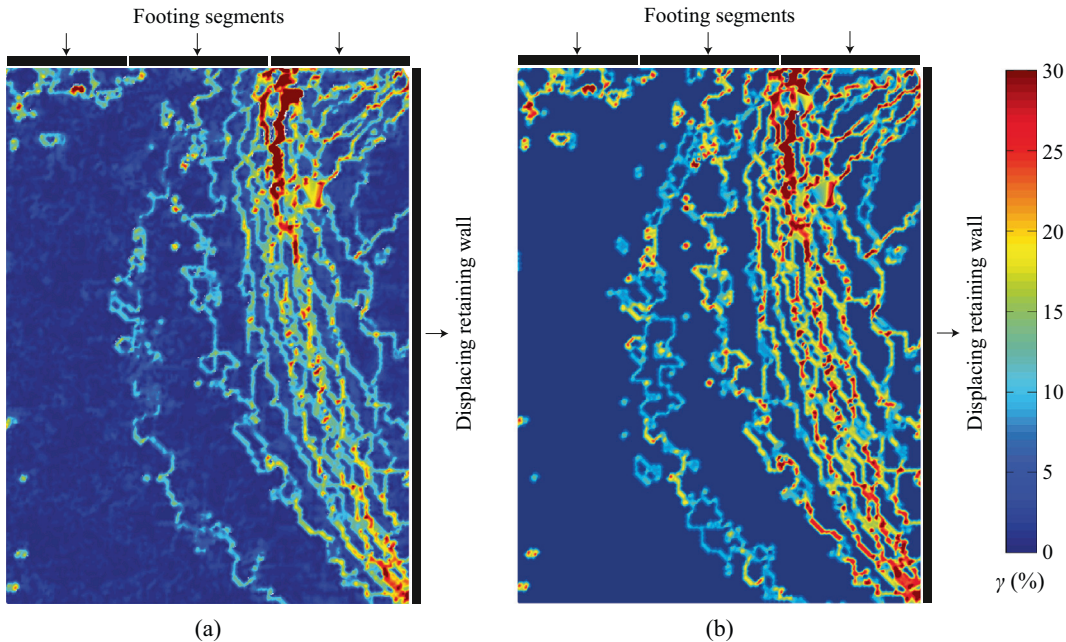


Fig. 13. Vermiculation identified in a model test of wall translation with surface footing load [15]: distribution of engineering shear strain shown (a) with and (b) without sub-pixel interpolation.

The original images analysed by Muir Wood and Leśniewska [15] were re-analysed for this paper using GeopIV. Analyses, using $L_s = 48p$ and $s = 12p$, reproduce vermiculate patterns very similar to those shown by Muir Wood and Leśniewska [15], with minor differences resulting from the precise location of the PIV/DIC subsets distributed across the images (Fig. 13).

Further analyses performed with different values of subset size, L_s , and spacing, s , indicated that the locations of the vermiculate features were insensitive to L_s but that the strain level in these features was highly dependent upon the spacing, s , because strain is derived as a function of the gradient of displacement (rule R5) and the spacing s provides the gauge length for strain calculation.

In this experiment the apparent particle to pixel ratio was $d/p \sim 10$, which would ordinarily indicate, according to Fig. 7, that 'peak locking' would not occur. However, there are a number of other potential causes for the bias errors that cause the 'peak locking' effect seen in Fig. 13(a). One possibility relates to the quality of the image texture. To demonstrate this, images of a similar experiment, using the same apparatus and (unannealed) granular material permitting better image texture,² were processed using the same analysis parameters. The engineering shear strain fields were again calculated from the displacement fields to sub-pixel and integer-pixel resolution and are shown in Fig. 14. There are now fewer vermiculate features in the engineering shear strain fields where the displacements were refined to sub-pixel resolution (Fig. 14(a)) indicating that the sub-pixel refinement process is generally functioning quite well. The feature immediately beneath the left edge of the footing (which remains even with sub-pixel interpolation, Fig. 14(a)) may be spurious but this is a position in which localisation of strains is quite likely and the gradient of deformation is high. The improved image texture has suppressed the potential emergence of vermiculate features in the far-field.

The image texture in the subsets used to create Fig. 13 was of low contrast. As a result the simple sub-pixel interpolation process

has an insignificant effect on the calculated displacements which are all essentially integer pixel magnitudes: there is negligible difference between Fig. 13(a) and (b). This, combined with the large overlaps of subsets, leads to extreme strain localisation in these vermiculate features as a consequence of 'peak locking'.

How well the sub-pixel refinement process is working in these analyses can be quantified graphically by plotting histograms of the magnitudes of the displacement components, as illustrated in Fig. 15. Here, the frequencies have been normalised by $\sum n$ (where n is the number of measurement points), because the different analyses used different numbers of subsets. It is clear that bias errors and 'peak locking' are occurring in both analyses, though to a much greater extent for the experiment with poor image texture (Figs. 13 and 15(a)) than that with improved image texture (Figs. 14 and 15(b)).

The quality of the image texture has a strong effect on computation precision [21,28] and ought to be checked by calculating a measure of (i) global image quality via Mean Intensity Gradient (MIG) following Pan et al. [18], as set out by rule R1, and/or (ii) subset image quality by calculating the standard deviation of subset pixel intensities, σ_{I_s} [28] or the Sum of Square of Subset Intensity Gradients (SSSIG) [21], as set out by rule R2. The values of σ_{I_s} and SSSIG for typical subsets confirm the importance of checking image texture quality (see Fig. 16). The image texture in the experiment where vermiculation was observed (Fig. 13) was sub-optimal (Fig. 16(a)), contravening rules R1 and R2. In contrast, the image texture for the improved experiment, where the bias errors were less significant (Fig. 14), was comparable to that for a geomaterial with optimised image texture [28] (compare Fig. 16(b) and (c)), so it was initially surprising that bias errors were still evident in the analysis of this image pair.

Persistent errors may also result if the magnitudes of deformation are too large. In both experiments the deformation imposed between the image pairs was relatively large (as indicated by engineering shear strains $\gamma > 30\%$) leading to probable contravention of R6, and potentially, if the subset shape function were found to be of lower-order than the subset deformation that is being measured, also rule R4. To check how these two effects were

² A different digital camera was also used in this experiment, however, it was of similar resolution to that used in the other experiment reported. Thus, the improvement in image texture evident in this experiment is thought to be due to the glass beads being left in their virgin, unannealed state.

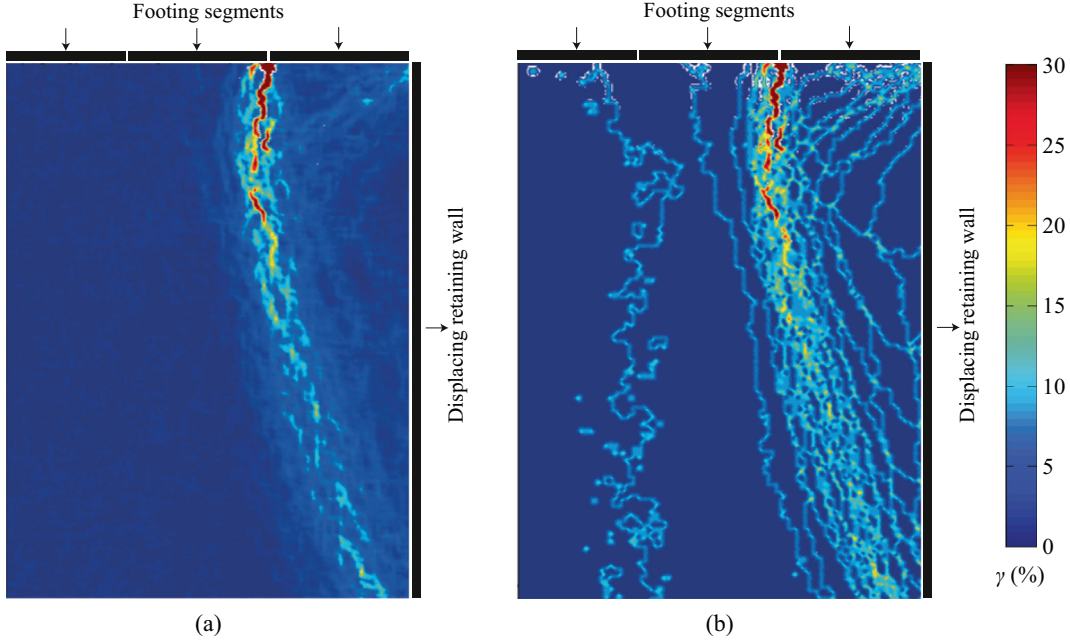


Fig. 14. Increment of wall displacement: distribution of engineering shear strain shown (a) with and (b) without sub-pixel interpolation [12]:

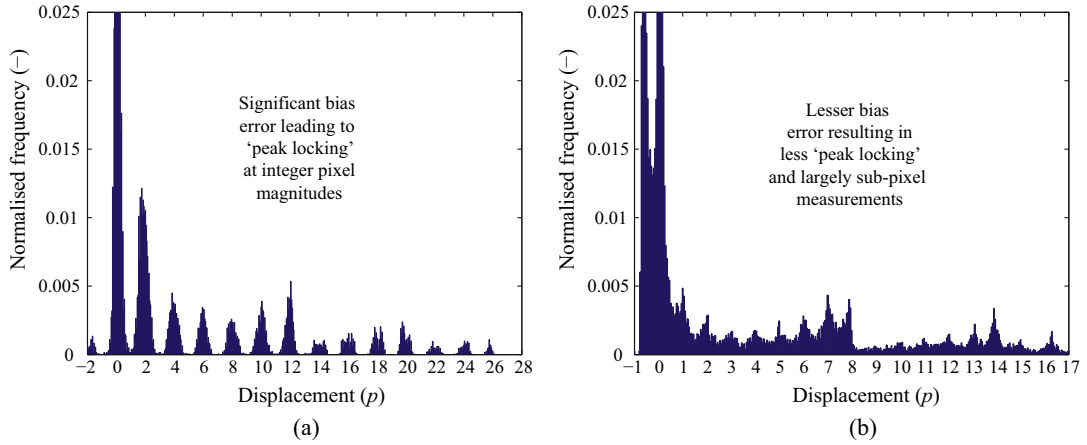


Fig. 15. Normalised histograms of displacement component magnitudes for model tests of wall/footing interaction: (a) clear vermiculation seen (Fig. 13 (b)) [15]; and (b) minimal vermiculation apparent (Fig. 14 (a)) [12].

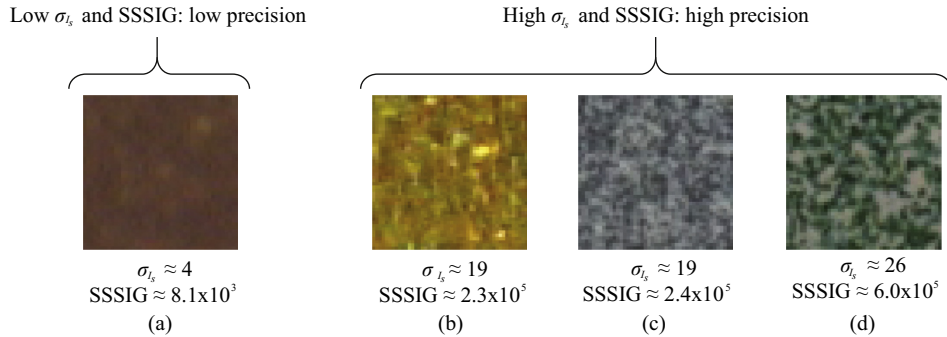


Fig. 16. Image texture for example subsets (48 × 48 pixels) and corresponding standard deviation of subset pixel intensities, σ_{ls} , and SSSIG for: (a) sub-optimal texture in a subset from the translating wall experiment reported by Muir Wood and Leśniewska [15]; (b) excellent texture in a subset from a similar translating wall experiment described by Leśniewska and Muir Wood [12] with comparable quality to (c) optimally seeded sand and (d) optimally seeded clay as reported by Stanier and White [28].

contributing to the errors the images from the two experiments were re-interpreted using GeoPIV-RG. The analysis settings adopted are summarised in Table 1.

The fields of engineering shear strain γ presented in Fig. 17(a and b) show that the vermiculate features are largely suppressed (c.f. Figs. 13 and 14 respectively), although there is more apparent

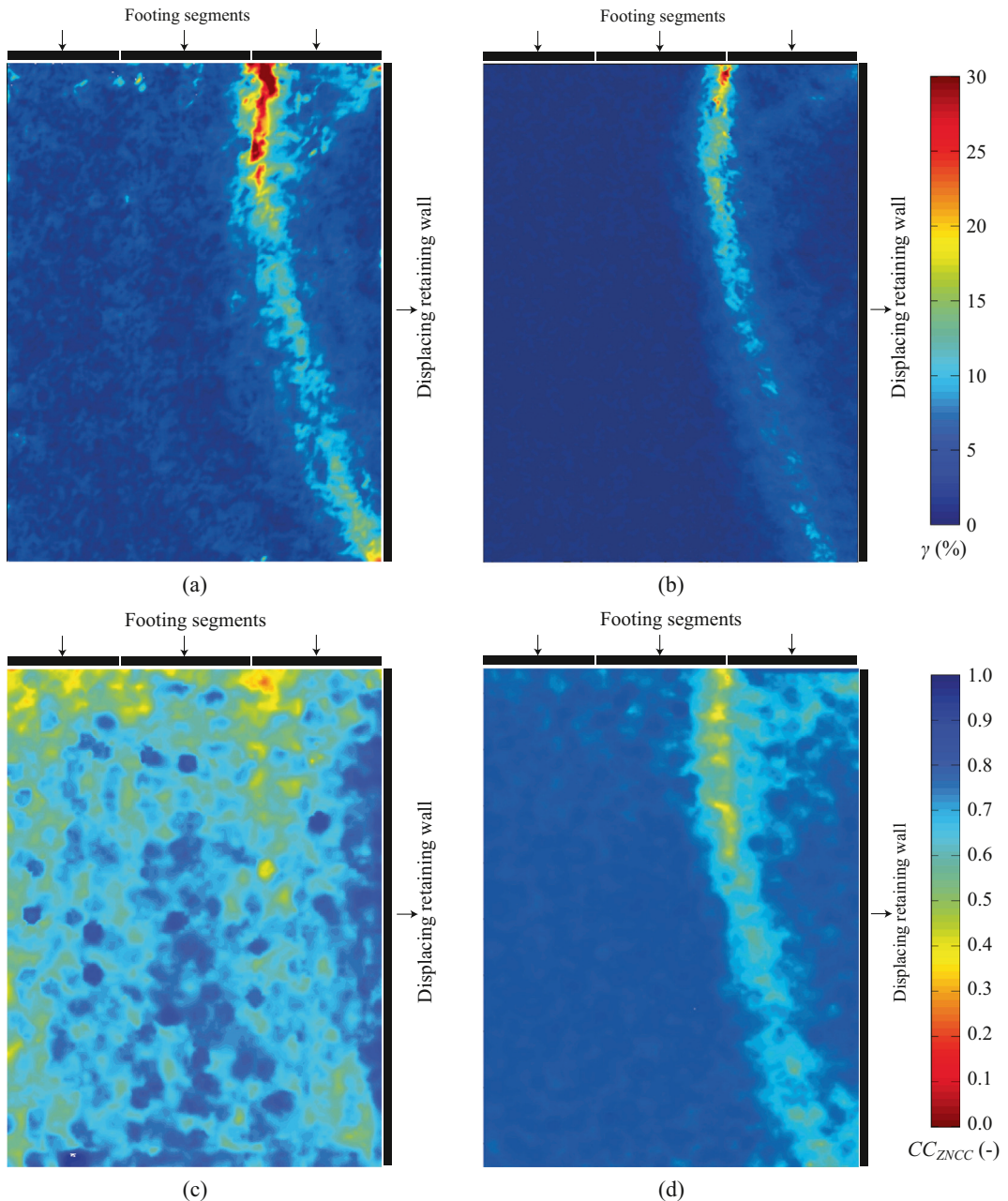


Fig. 17. Re-interpretation of the model tests of wall translation with surface footing load reported by (a and c) Muir Wood and Leśniewska [15] and (b and d) Leśniewska and Muir Wood [12] using GeoPIV-RG: (a and b) engineering shear strain, γ ; and (c and d) optimal cross-correlation coefficient, CC_{ZNCC} .

noise than was seen in the analyses of the ‘perfect’ synthetic images. The optimised values of the cross-correlation coefficient CC_{ZNCC} in Fig. 17(c and d) provide a check on the quality of the match between the locations of the subsets in the ‘reference’ and ‘target’ images after sub-pixel refinement. In the benchmarking of GeoPIV-RG, Stanier et al. [27] suggest that a minimum value of $CC_{ZNCC} = 0.75$ results in reliable displacement measurements that are practically unaffected by the loss of correlation caused by deformation. If the same criteria were applied to the analysis with clear vermiculations (Fig. 17(a and c)) 86% of the measurement points would be discarded. In contrast, for the analysis with better image texture (Fig. 17(b and d)) only 22% of the measurement points would be discarded by applying the same criterion, and most of these data points clearly lie in the region

of intense straining swooping down from the edge of the footing. Evidently the better image texture leads to improved correlation and reduction in associated measurement errors.

Normalised histograms of the displacement components shown in Fig. 18 (comparable to Fig. 15) illustrate that for both experiments the bias errors are almost completely eradicated by the use of the first-order subset shape function of GeoPIV-RG. This supports the hypothesis that such higher order functions can be used for accurate determination of larger deformations than can zero-order methods which use correlation peak interpolation for sub-pixel refinement.

To show (i) that these erroneous vermiculate features are amplified by increased overlapping when using GeoPIV, and (ii) that GeoPIV-RG is less susceptible to ‘peak locking’ for real data,

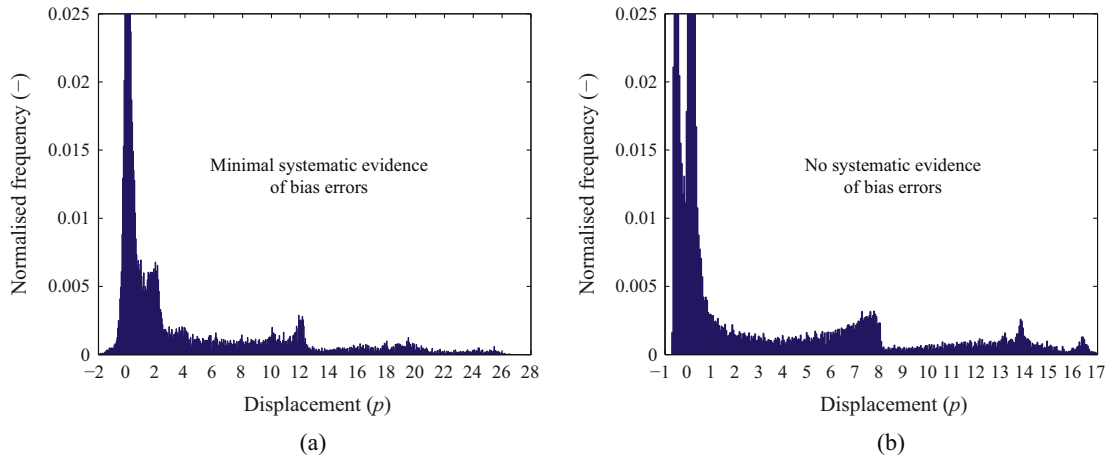


Fig. 18. Histograms of displacement component magnitudes for model tests of wall translation with surface footing load, re-analysed using GeoPIV-RG, for the model tests reported by: (a) Muir Wood and Leśniewska [15] and (b) Leśniewska and Muir Wood [12] (c.f. Fig. 15(a) and (b) respectively).

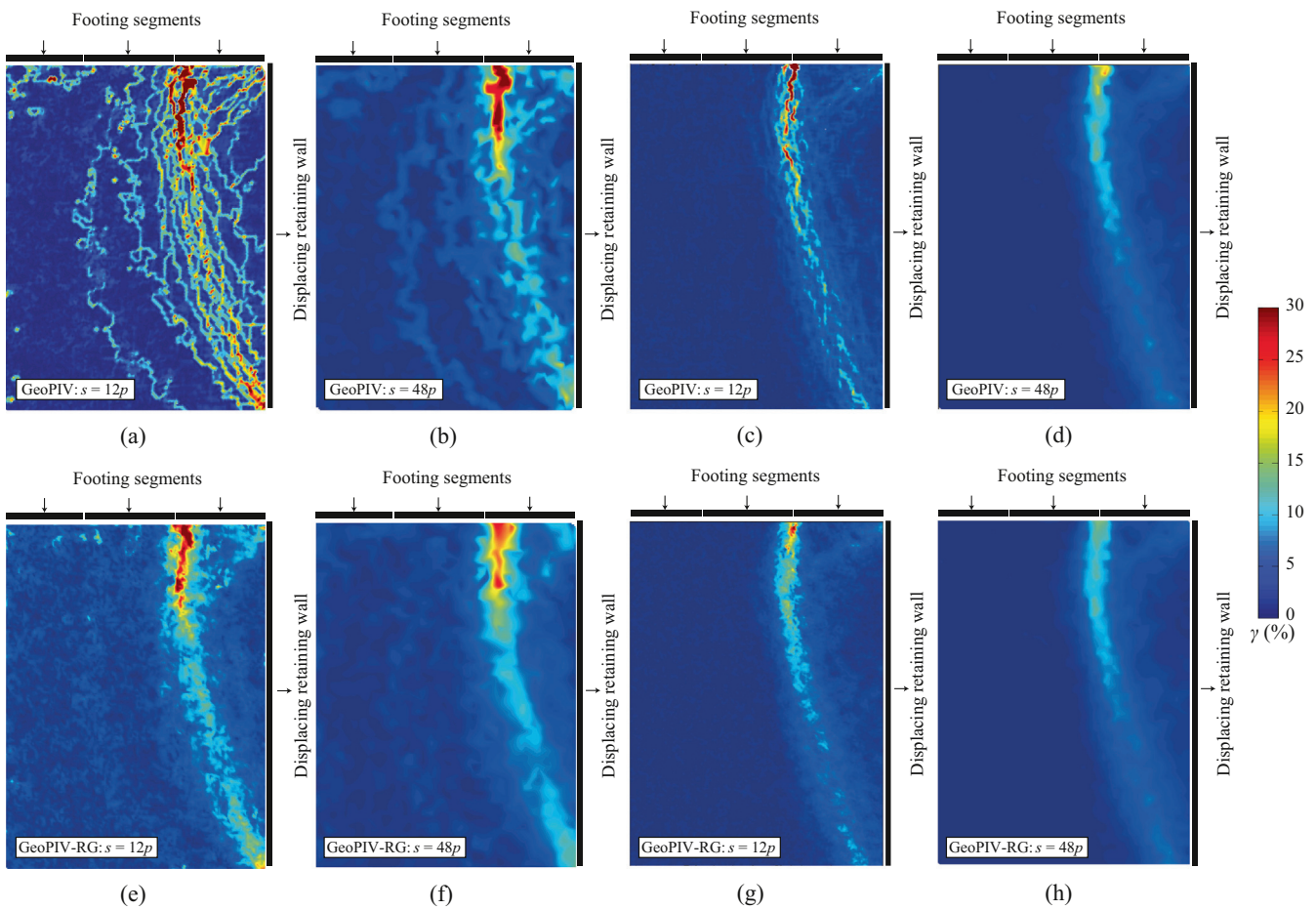


Fig. 19. Engineering shear strain fields, γ , for the model tests of wall rotation with surface footing load described by (a, b, e, f) Muir Wood and Leśniewska [15] and (c, d, g, h) Leśniewska and Muir Wood [12] for (a, c, e, g) subset spacing $s = 12$, overlap ratios $((L_s - s)/L_s) = 0.75$; and (b, d, f, h) subset spacing $s = 48$, overlap ratios $((L_s - s)/L_s) = 0$; computed using (a-d) GeoPIV and (e-h) GeoPIV-RG.

a series of additional analyses with spacing $s = 48p$ (corresponding to overlapping ratio $((L_s - s)/L_s) = 0$) were performed. The resulting engineering shear strain fields are presented in Fig. 19, side-by-side with those for $s = 12p$ (corresponding to overlap ratio of 0.75). For the model test reported by Muir Wood and Leśniewska [15], where the 'peak-locking' was extreme, the vermiculate

features are still apparent for the zero-order GeoPIV analyses, even for $s = 48p$; only the magnitude of the features has changed (because the strain is calculated from the ratio of displacement step to subset spacing). In contrast, for the model test reported by Leśniewska and Muir Wood [12], where the 'peak-locking' was moderate, increasing the subset spacing (and thus reducing

the overlap ratio) results in the masking of bias errors, as suggested by rule R5. For GeoPIV-RG the vermiculate features are suppressed for all cases, though it appears that detail is lost when the subset overlapping is reduced so that $s = 48p$. There are no major disadvantages in using quite large degrees of overlap in order to extract more detailed observations, so long as the underlying subset shape function is able to describe the deformations that have occurred.

6. Conclusions

This paper has explored the possibility that vermiculate features observed in image analyses of some experiments involving deformation of granular materials might be spurious artefacts. Analyses of synthetic images, and reinterpretation of image pairs from experiments using state-of-the-art image analysis algorithms, have demonstrated that the vermiculate features are almost certainly the product of a combination of both the experimental setup and shortcomings in the image analysis algorithms originally employed.

The studies of synthetic and real images of granular materials have demonstrated that an improvement of performance can be obtained using computationally more intensive algorithms which apply higher order shape functions to describe the deformations occurring within the analysis subsets. However, while such algorithms can suppress the appearance of spurious vermiculate features, the quality of the resulting measurements is still compromised if the image texture is of sub-optimal quality. If the particles are too small or are not easily distinguished from the background, then their movement cannot be reliably detected no matter how sophisticated the subsequent image analysis. The resulting bias errors become more dramatic when strains are calculated from derivatives of the displacements. Subset overlapping can also lead to the amplification of resulting errors and, in some cases, to the generation of spurious strain features.

There are several specific recommendations:

1. Choose seeding particles that are of sufficient diameter within the images captured for each experimental setup (i.e. $d/p > 4$).
2. Seed the exposed plane of geotechnical models with dyed sand or modelling flock such that $0.3 < \text{ASR} < 0.7$, so as to ensure that an optimal amount of seeding is applied to each model.
3. Evaluate the quality of the images to be analysed using appropriate statistical measures of image texture quality (e.g. MIG, SSSIG and σ_{I_s}).
4. Inspect the histogram of displacements to ensure no integer pixel bias.
5. Make use of image analysis software that incorporates higher-order subset deformation functions.
6. Explore the effect of varying the spacing of correlation subsets.
7. Confirm the mechanical plausibility of the patterns of displacement and strain that emerge from the image analysis.

Users of advanced image correlation techniques need to be aware that spurious numerical artefacts can be unwittingly generated in the computed strain fields. Such awareness should then prompt them to consider the potential for introduction of improvements at all stages of the image acquisition and processing chain. Guidance has been given concerning details of the experimental equipment and procedures and concerning the selection and application of the image analysis algorithms. As is often the case, apparently simple-to-use but sophisticated programs contain hidden traps for the unwary.

Acknowledgements

The work forms part of the activities of the Centre for Offshore Foundation Systems (COFS) at the University of Western Australia,

which is supported by the Lloyd's Register Foundation as a Centre of Excellence and is a node of the Australian Research Council (ARC) Centre of Excellence in Geotechnical Science and Engineering. Jim Hambleton was seconded to University of Western Australia under the aegis of the ARC Centre of Excellence in Geotechnical Science and Engineering. Jelke Dijkstra is supported by an Intra-European Fellowship EC/FP7-MC-IEF 623613 EMPIRC. Danuta Leśniewska was supported by NCN Grant No. 2011/03/B/ST8/05865. David White holds the Shell Energy and Minerals Institute (EMI) Chair in Offshore Engineering. David Muir Wood is particularly grateful for the support of the Centre for Offshore Foundation Systems, University of Western Australia through the award of the Martin Fahey Visiting Fellowship during 2013. He also acknowledges the support of the Northern Research Partnership of Scottish universities at Dundee University and the invaluable support of the British Council in making initial experimental contacts for photoelastic and image analysis of granular materials.

Appendix A. Definitions of image analysis variables

For completeness the various variables that have been mentioned are briefly defined here.

The zero normalised cross-correlation coefficient (CC_{ZNCC}) is defined as:

$$\text{CC}_{\text{ZNCC}} = \frac{\sum_{i,j \in n_s} (I_{ij}^r - \bar{I}^r)(I_{ij}^t - \bar{I}^t)}{\sqrt{\sum_{i,j \in n_s} [I_{ij}^r - \bar{I}^r]^2 \sum_{i,j \in n_s} [I_{ij}^t - \bar{I}^t]^2}} \quad (1)$$

where I_{ij}^r and I_{ij}^t are the pixel intensities for a given i, j coordinate in the 'reference' and 'target' images respectively. The mean pixel intensities for the 'reference' and 'target' images, \bar{I}^r and \bar{I}^t are calculated as

$$\bar{I}^r = \frac{1}{n_s} \sum_{i,j \in n_s} I_{ij}^r; \quad \bar{I}^t = \frac{1}{n_s} \sum_{i,j \in n_s} I_{ij}^t \quad (2)$$

where n_s is the number of pixels in the subset.

The Signal to Noise Ratio SNR is defined as:

$$\text{SNR} = \frac{I_{\text{signal}}}{I_{\text{noise}}} \quad (3)$$

where I_{signal} and I_{noise} are the intensity components representing the signal and the noise respectively.

The Mean Intensity Gradient MIG is defined (after Pan et al. [18]) as:

$$\text{MIG} = \sum_{i,j \in n_l} \frac{1}{n_l} \sqrt{(I_x')^2 + (I_y')^2} \quad (4)$$

where I_x' and I_y' are the intensity gradients in the x and y directions respectively and n_l is the number of pixels in the image.

The Artificial Seeding Ratio ASR is defined (after Stanier and White [28]) as:

$$\text{ASR} = \frac{\bar{I} - \bar{I}_{\text{ASR}=0}}{\bar{I}_{\text{ASR}=1} - \bar{I}_{\text{ASR}=0}} \quad (5)$$

where \bar{I} is the mean pixel intensity of the image, $\bar{I}_{\text{ASR}=0}$ is the mean pixel intensity for an image with no artificial seeding and $\bar{I}_{\text{ASR}=1}$ is the mean pixel intensity for an image with saturated artificial seeding.

The standard deviation of the subset pixel intensities σ_{I_s} is computed as:

$$\sigma_{I_s} = \sqrt{\frac{1}{n_s} \sum_{i,j \in n_s} (I_{ij} - \bar{I})^2} \quad (6)$$

where I_{ij} and \bar{I} are the pixel and mean subset pixel intensities respectively and n_s is the number of pixels in the subset.

The Sum of Squares of Subset pixel Intensity Gradients (SSSIG) are defined (after Pan et al. [21]) as:

$$\text{SSSIG}_x = \sum_{ij \in n_s} (I'_x)^2 \quad (7)$$

$$\text{SSSIG}_y = \sum_{ij \in n_s} (I'_y)^2 \quad (8)$$

where I'_x and I'_y are as defined previously and n_s is the number of pixels in the subset.

The intensity of each pixel in the artificial images was generated using the following function:

$$I_{ij} = \min \left(\sum_{n=1}^{n_p} C \exp \left(\frac{-(i - x_p(n))^2 - (j - y_p(n))^2}{(d_p/2)^2} \right), 255 \right) \quad (9)$$

where I_{ij} is the intensity of the pixel in row i and column j of the artificial image, n_p is the total number of projected dots and n is the n th projected dot. C is the contrast of the dots in the range of 0–255 (in this instance C was taken as 200), $x_p(n)$ and $y_p(n)$ are the coordinates of the n th dot (taken as the central pixel for the single dot in the images in Fig. 6 and randomly generated for each of the dots in the images in Fig. 9) and d_p is the diameter of the projected dots. The intensity of each pixel I_{ij} was capped at 255 since that is the maximum brightness of a pixel in an 8-bit digital image.

References

- [1] Adrian R, Westerweel J. Particle image velocimetry. Cambridge University Press; 2011.
- [2] Anastasopoulos I, Gazetas M, Bransby M, Davies M, El Nahas A. Fault rupture propagation through sand: finite-element analysis and validation through centrifuge experiments. *J Geotech GeoEnviron Eng* 2007;133:943–58.
- [3] Ando E, Hall S, Viggiani G, Desrues J, Bésuelle P. Grain-scale experimental investigation of localised deformation in sand: a discrete particle tracking approach. *Acta Geotech* 2012;7(1):1–13.
- [4] Bhandari A, Powrie W, Harkness R. A digital image-based deformation measurement system for triaxial tests. *ASTM Geotech Test J* 2012;35 (2):209–26.
- [5] Blaber J, Adair B, Antoniou A. Ncorr: open-source 2d digital image correlation matlab software. *J Exp Mech*; 2015, published ahead of print online.
- [6] Cosman P, Gray R, Olshen R. Evaluating quality of compressed medical images: SNR, subjective rating, and diagnostic accuracy. *Proc IEEE* 1994;82(6):919–32.
- [7] Crocker J, Grier D. Methods of digital video microscopy for colloidal studies. *J Colloid Interface Sci* 1996;179(1):298–310.
- [8] Flamant A. Sur la réparation des pressions dans un solide rectangulaire chargé transversalement. *Comptes Rendus de l'Académie des Sciences* 1892;114: 1465–8.
- [9] Hall S, Bornert M, Desrues J, Pannier Y, Lenoir N, Viggiani G, et al. Discrete and continuum analysis of localised deformation in sand using X-ray μ crt and volumetric digital image correlation. *Géotechnique* 2010;60(5):315–22.
- [10] Keshavarzy A, Ball J. An application of image processing in the study of sediment motion. *J Hydraul Res* 1999;37(4):559–76.
- [11] Lee C, Take W, Hoult N. Optimum accuracy of two-dimensional strain measurements using digital image correlation. *J Comput Civil Eng* 2012;26: 795–803.
- [12] Leśniewska D, Muir Wood D. Observations of stresses and strains in a granular material. *J Eng Mech* 2009;135(9):1038–54.
- [13] Lewis J. Fast normalized cross-correlation. *Vis Interface* 1995;10(1):120–3.
- [14] Marshall A, Farrel R, Klar A, Mair R. Tunnels in sands: the effect of size, depth and volume loss on greenfield displacements. *Géotechnique* 2012;62 (5):385–99.
- [15] Muir Wood D, Leśniewska D. Discussion: heterogeneity and soil element testing. *Géotech Lett* 2012;2(5):217–9.
- [16] Nazhat Y, Airey D. The kinematics of granular soils subjected to rapid impact loading. *Granul Matter* 2015;17(1):1–20.
- [17] Pan B, Li K, Tong W. Fast, robust and accurate digital image correlation calculation without redundant computations. *Exp Mech* 2013;53(7):1277–89.
- [18] Pan B, Lu Z, Xie H. Mean intensity gradient: an effective global parameter for quality assessment of the speckle patterns used in digital image correlation. *Opt Lasers Eng* 2010;48(4):469–77.
- [19] Pan B, Wu D, Xia Y. Incremental calculation for large deformation measurement. *Opt Lasers Eng* 2012;50:586–92.
- [20] Pan B, Xie H, Wang Z. Equivalence of digital image correlation criteria for pattern matching. *Appl Opt* 2010;49(28):5501–9.
- [21] Pan B, Xie H, Wang Z, Qian K, Wang Z. Study on subset size selection in digital image correlation for speckle patterns. *Opt Express* 2008;16(10):7037–48.
- [22] Raffel M, Willert C, Wereley S, Kompenhans J. Particle image velocimetry: a practical guide. Springer; 2007.
- [23] Rechenmacher A, Finno R. Digital image correlation to evaluate shear banding in dilative sands. *Geotech Test J* 2004;27(1):1–10.
- [24] Rosenbrand E, Dijkstra J. Application of image subtraction data to quantify suffusion. *Géotech Lett* 2012;2:37–41.
- [25] Scarano F. Tomographic PIV: principles and practice. *Meas Sci Technol* 2013;24(1):012001.
- [26] Schreier H, Sutton M. Systematic errors in digital image correlation due to under matched subset shape functions. *J Exp Mech* 2002;42(3):303–10.
- [27] Stanier S, Blaber J, Take W, White D. Improved image-based deformation measurement for geotechnical applications. *Can Geotech J* 2015. <http://dx.doi.org/10.1139/cgj-2015-0253>.
- [28] Stanier S, White D. Improved image-based deformation measurement in the centrifuge environment. *ASTM Geotech Test J* 2013;36(6):915–28.
- [29] Stelzer E. Contrast, resolution, pixelation, dynamic range and signal-to-noise ratio: fundamental limits to resolution in fluorescence light microscopy. *J Microsc* 1998;189(1):15–24.
- [30] Sutton M. Digital image correlation for shape and deformation measurements. In: Sharpe Jr W, editor. *Springer handbook of experimental solid mechanics*. Springer; 2008. Chapter 20.
- [31] Sutton M, Wolters W, Peters W, Ranson W, McNeill S. Determination of displacements using an improved digital correlation method. *Image Vis Comput* 1983;1(3):133–9.
- [32] Sveen J. An introduction to MATPIV v. 1.6. 1. Eprint no. 2, issn 0809-4403, Dept. of Mathematics, University of oslo; 2004.
- [33] Take W, Bolton M. Identification of seasonal slope behaviour mechanisms from centrifuge case studies. In: Proceedings of the conference on advances in geotechnical engineering: the skempton conference; 2004. p. 992–1004.
- [34] Taylor Z, Gurka R, van Kopp G, Liberzon A. Long-duration time-resolved PIV to study unsteady aerodynamics. *IEEE Trans Instrum Meas* 2010;59(12):3262–9.
- [35] Thielicke W, Stamhuis E. PIVlab—towards user-friendly, affordable and accurate digital Particle Image Velocimetry in MATLAB. *J Open Res Softw* 2014;2(1):e30.
- [36] Tong W. An evaluation of digital image correlation criteria for strain mapping applications. *Strain* 2005;41(4):167–75.
- [37] Vennemann P. JPIV online manual: <<http://www.jpiv.vennemann-online.de>>; 2015.
- [38] Westerweel J. Fundamentals of digital particle image velocimetry. *Meas Sci Technol* 1997;8(12):1379.
- [39] Westerweel J. Effect of sensor geometry on the performance of PIV interrogation. In: Laser techniques applied to fluid mechanics. Springer; 2000. p. 37–55.
- [40] White D, Bolton M. Displacement and strain paths during plane-strain model pile installation in sand. *Géotechnique* 2004;54(6):375–97.
- [41] White D, Take W, Bolton M. Soil deformation measurement using particle image velocimetry (PIV) and photogrammetry. *Géotechnique* 2003;53 (7):619–31.
- [42] Yu L, Pan B. The errors in digital image correlation due to overmatched shape functions. *Meas Sci Technol* 2015;045202:1–9.